JGR Atmospheres

RESEARCH ARTICLE
10.1029/2020JD033870

Idealized Model Simulations to Determine Impacts of Storm-Relative Winds on Differential Reflectivity and Specific Differential Phase Fields

Scott D. Loeffler[1] **and Matthew R. Kumjian**[1]

[1]Department of Meteorology and Atmospheric Science, The Pennsylvania State University, University Park, PA, USA

Key Points:

- Observed polarimetric size sorting signatures can be used to gain insight into the storm-relative winds
- Separation between enhanced polarimetric variables is well-correlated with the magnitude and alignment of the mean storm-relative wind
- The magnitude and orientation of this separation can be related to the storm-relative helicity in the sorting layer

Correspondence to:
S. D. Loeffler,
swl5295@psu.edu

Citation:
Loeffler, S. D., & Kumjian, M. R. (2020). Idealized model simulations to determine impacts of storm-relative winds on differential reflectivity and specific differential phase fields. *Journal of Geophysical Research: Atmospheres*, *125*, e2020JD033870. https://doi.org/10.1029/2020JD033870

Received 9 SEP 2020
Accepted 21 NOV 2020

Abstract Hydrometeors of varying sizes have different fall speeds; for example, larger raindrops have greater fall speeds than smaller raindrops. The resultant differential sedimentation leads to differences in residence time in a sorting layer where drops can be advected by the storm-relative winds. The resulting size sorting has an effect on the polarimetric radar variables including specific differential phase K_{DP} and differential reflectivity Z_{DR}. This study uses a simple numerical model of raindrop size sorting to analyze and further elucidate the relationship between the storm-relative winds and the Z_{DR} and K_{DP} fields. Increased mean storm-relative winds lead to increased Z_{DR} magnitudes and decreased K_{DP} magnitudes. The separation distance between Z_{DR} and K_{DP} maxima is proportional to the magnitude of the mean storm-relative wind and the orientation of a vector from Z_{DR} to K_{DP} maxima is aligned with the mean storm-relative wind over the sorting layer. Further, it is shown that larger values of storm-relative helicity are associated with greater separation distances and separation orientations approaching orthogonal to the shear vector over the sorting layer.

Plain Language Summary Raindrops of different sizes fall at different speeds, such that larger raindrops fall faster and spend less time in a given layer of the atmosphere than smaller raindrops. This feature has an effect on the polarimetric radar variables, two of which are the focus of this study. This study uses a simple model to analyze the relationship between the two radar variables and the winds in a given layer. Changes in the winds in a given layer lead to changes in the magnitudes of these radar variables, as well as the separation between high values of the two variables. Further, it is shown that the magnitude and orientation of this separation can be used to estimate parameters of the wind profile.

1. Introduction

As clouds begin to precipitate, there are several different microphysical processes that can change the drop size distribution (DSD) as the drops fall out, such as evaporation, breakup, and coalescence. The DSDs can also evolve due to hydrometeor size sorting arising from differential sedimentation. Terminal velocities of raindrops increase with increasing size (e.g., Beard, 1976; Brandes et al., 2002; Foote & du Toit, 1969; R. Gunn & Kinzer, 1949) so that larger drops fall through a given layer more rapidly than smaller drops. Larger drops will reach the surface before smaller drops, so there will be an initial sorting of raindrops by size with progressively smaller drops located higher above the surface. However, after some time (assuming steady-state conditions aloft), the smaller drops will reach the surface and there will no longer be a separation of different drop sizes. This transient size sorting from initial differential sedimentation lasts on the order of 5–10 min (Kingfield & Picca, 2018).

There are mechanisms that will maintain this size sorting beyond this initial transient effect, as described in Kumjian and Ryzhkov (2012), hereafter K12. One of these mechanisms is an updraft, where only larger raindrops with sufficiently large terminal velocities can overcome the strength of the updraft and descend to the surface. Another mechanism, and the focus of this study, is storm-relative flow located in the layer through which the drops descend. These storm-relative winds are the fundamental mechanism for this type of size sorting (Dawson et al., 2015, hereafter D15) and not shear or storm-relative helicity (SRH) as previous studies had suggested (e.g., K. Gunn & Marshall 1955; Kumjian & Ryzhkov, 2009). Larger drops with faster fall speeds fall through a sorting layer more quickly compared to smaller drops with slower fall speeds. The decreased time in a sorting layer leads to the larger drops being advected a shorter distance downwind

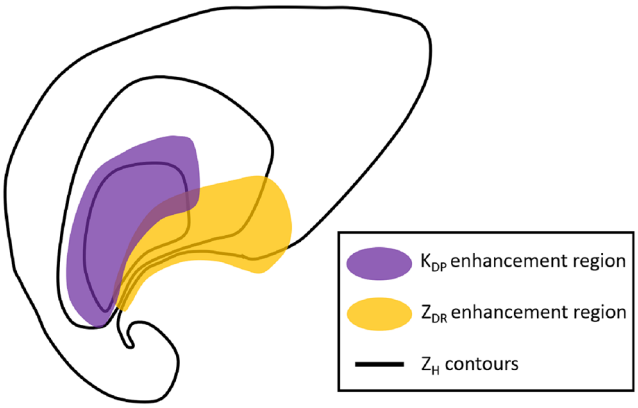

Figure 1. Schematic showing the Z_{DR}–K_{DP} size sorting signature in a supercell. Enhanced regions of K_{DP} and Z_{DR} are shown in the forward flank (purple and yellow, respectively). Contours of Z_H are shown at 30, 40, and 50 dBZ (black lines).

from their source region compared to smaller drops. This results in a horizontal sorting of drops by size where larger drops are found closer to the source region and smaller drops are found farther downwind. Early works by Marshall (1953) and K. Gunn and Marshall (1955) showed that the fastest falling hydrometeors were found toward the leading edge (i.e., the upwind side in a storm-relative sense) of a sheared precipitation region. Marshall (1953) observed falling snow aggregates and noted the "mare's tail" trajectories for particles falling through a layer with wind shear, while K. Gunn and Marshall (1955) more rigorously analyzed the effects of wind shear on falling particles. Although these studies focused on wind shear, they mention either motion relative to the generating cell or the cell moving relative to the air around it, both of which imply the presence of storm-relative winds.

The changes to the DSDs owing to size sorting naturally have an effect on the polarimetric radar variables, as shown in K12, particularly differential reflectivity Z_{DR} and specific differential phase K_{DP}. Introduced by Seliga and Bringi (1976, 1978), Z_{DR} is the difference between horizontally and vertically polarized radar reflectivity factors using logarithmic units. For oblate raindrops with their major axis in the horizontal, Z_{DR} is positive, while Z_{DR} approaches zero as raindrops become more spherical. As raindrops grow larger they become more oblate. Because of this, Z_{DR} can be used to estimate the median drop size in the sampling volume, where larger Z_{DR} values imply the presence of larger raindrops. Although Z_{DR} is not sensitive to number concentration, K_{DP} is. Further, compared to Z_{DR}, K_{DP} is more closely related to the mass of the raindrops: it is proportional to the ~4th to 5th moment of the DSD (Kumjian et al., 2019; Sachidananda & Zrnić, 1986). K_{DP} is usually expressed in deg km^{-1} and represents the difference per unit distance in phase shifts between horizontally and vertically polarized waves. K_{DP} is also less sensitive to drop size compared to radar reflectivity factor Z_H. K_{DP} is closely related to the rainfall rate (Sachidananda & Zrnić, 1986) where enhanced values of K_{DP} are associated with heavy precipitation. For a detailed review of the polarimetric radar variables, see Kumjian (2013).

Size sorting by storm-relative winds leads to a horizontal separation where relatively larger concentrations of smaller drops are found farther downwind from the source region than sparser concentrations of larger drops. In this case, the mean storm-relative wind is directed from the area of relatively larger drops toward the region of relatively smaller drops. This region of larger drops will have greater Z_{DR} values owing to the larger median drop size and decreased Z_H owing to part of the drop size spectrum (i.e., smaller drops) being removed. The region of relatively smaller drops will have smaller Z_{DR} values because of decreased drop size, but these drops are still large and nonspherical enough to produce a differential phase shift. These drops are in larger concentrations, leading to larger K_{DP} values. Thus, a separation between areas characterized by enhanced Z_{DR} and K_{DP} is created.

These regions of enhanced Z_{DR} and K_{DP} have been studied in several past works. Ryzhkov et al. (2005) observed an area of increased Z_{DR} values at the lower levels along the inflow edge of the supercell forward flank, which Kumjian and Ryzhkov (2008) later termed the "Z_{DR} arc." Palmer et al. (2011) noted Z_{DR} arcs with values >8 dB collocated with $Z_H < 25$ dBZ at C-band. Dawson et al. (2014) concluded that the two main mechanisms for large Z_{DR} values at low levels were melting of small hail and graupel (which can provide a source for large drops), and size sorting (which preferentially removes small drops from the volume), where the gradient of Z_{DR} values depended on the alignment of the mean storm-relative wind vector through the layer in which the hydrometeors descend. Romine et al. (2008) observed a region of high K_{DP} values located further inside the forward flank of supercells, which they termed the "K_{DP} foot." This region of enhanced K_{DP} tends to be co-located with enhanced Z_H in the forward flank of supercells (Kumjian & Ryzhkov, 2008). A schematic showing the separation of these enhanced Z_{DR} and K_{DP} regions is shown in Figure 1.

Because of the connection to the storm-relative winds, a few recent studies have analyzed the enhanced regions of both Z_{DR} and K_{DP} in an attempt to gain information about the storm dynamics and environment. Crowe et al. (2012) studied the separation between enhanced Z_{DR} and K_{DP} regions in different convective

modes in the southeastern United States. One finding from their study was that while nontornadic storms tended to have the two enhanced regions overlapping, tornadic storms tended to show greater separation between the two enhanced regions. However, most of the analysis was qualitative in nature and was performed on a relatively small sample set. Martinaitis (2017) analyzed this separation, also in a qualitative manner, as a part of the author's radar analysis of convection associated with land-falling tropical systems in Florida. When comparing tornadic and nontornadic storms, the author was unable to find any significant differences. Quantitative assessments of this Z_{DR}–K_{DP} separation in supercells (Jurewicz & Gitro, 2014) and nonsupercells (Loeffler & Kumjian, 2018) have also been performed. Loeffler and Kumjian (2018) used what they called the "separation vector" which is comprised of the separation distance and the orientation between the two enhanced regions. A recent study by Loeffler et al. (2020) showed that tornadic supercells tended to have separation orientations closer to perpendicular to storm motion, while nontornadic supercells tended to have orientations closer to parallel to storm motion.

The aim for this study is to assess the relationship between the storm-relative winds and the K_{DP} and Z_{DR} fields in order to provide additional clarification to arguments made in previous studies. In particular, here we parse out effects of separation distance and orientation focusing on the storm-relative winds and SRH. Currently, storm-relative winds and SRH are usually diagnosed from one of a few different methods. One method is through soundings launched by operational forecasters. However, these soundings are typically only launched twice a day and spread out around the country so that the closest sounding may be removed from a severe thunderstorm by hundreds of kilometers and several hours. Another method is the use of model soundings from numerical models such as the Rapid Refresh (RAP; Benjamin et al., 2016). These model soundings can have biases especially in the low levels (Thompson et al., 2003), which are important for convective processes such as tornadogenesis. Additionally, velocity-azimuth displays from Doppler velocity radar data can be used to estimate the vertical wind profile, but are contingent upon scatterers moving in uniform flow which may break down after convective initiation. Using polarimetric radar data provides consistent observations in real time to gain insight into the near-storm environment.

2. Data and Methods

2.1. Model Configuration

In order to assess the effects of storm-relative winds on low-level K_{DP} and Z_{DR} fields, we construct a simple 3-D numerical model similar to that in Laurencin et al. (2020). The model is also similar to the model used in K12, the main difference being that this model is expanded to three dimensions. Prescribed vertical wind profiles have both horizontal components, and we assume they are horizontally homogeneous. This is a steady-state model (i.e., no dependence on time) and, thus, is meant to capture this type of size sorting as opposed to the transient effect from differential sedimentation (K12). Only raindrops are considered in this model. We ignore any microphysical processes (e.g., evaporation, breakup, coalescence, etc.) to be consistent with previous works and to isolate the size sorting process (Kumjian & Ryzhkov, 2009; K12; D15). Further, we assume no changes in air density with height so there is no change in drop fall speed with height (e.g., Beard, 1976; Foote & du Toit, 1969; R. Gunn & Kinzer, 1949), which may lead to a small overestimation for separation distance of less than <10% and negligible differences in maximum K_{DP} and Z_{DR} magnitudes. While this study only focuses on the singular process of size sorting, past studies have shown that size sorting is a dominant process with respect to low-level polarimetric radar signatures (Dawson et al., 2014; Kumjian et al., 2015). Detailed modeling studies considering all rain microphysical processes have shown the polarimetric radar fingerprint from size sorting, when active, is dominant over those of the collisional processes (e.g., Kumjian & Prat, 2014; Kumjian et al., 2019). Further, simple models such as this one have been able to replicate a reasonable degree of observed signatures in supercells (D15) and hurricane eyewalls (Laurencin et al., 2020).

Due to the steady-state assumption and lack of microphysical processes, raindrop motion for each size bin is the result of advection and sedimentation only, shown by

$$u(z)\frac{\partial N(D)}{\partial x} + v(z)\frac{\partial N(D)}{\partial y} + v_t(D)\frac{\partial N(D)}{\partial z} = 0 \quad (1)$$

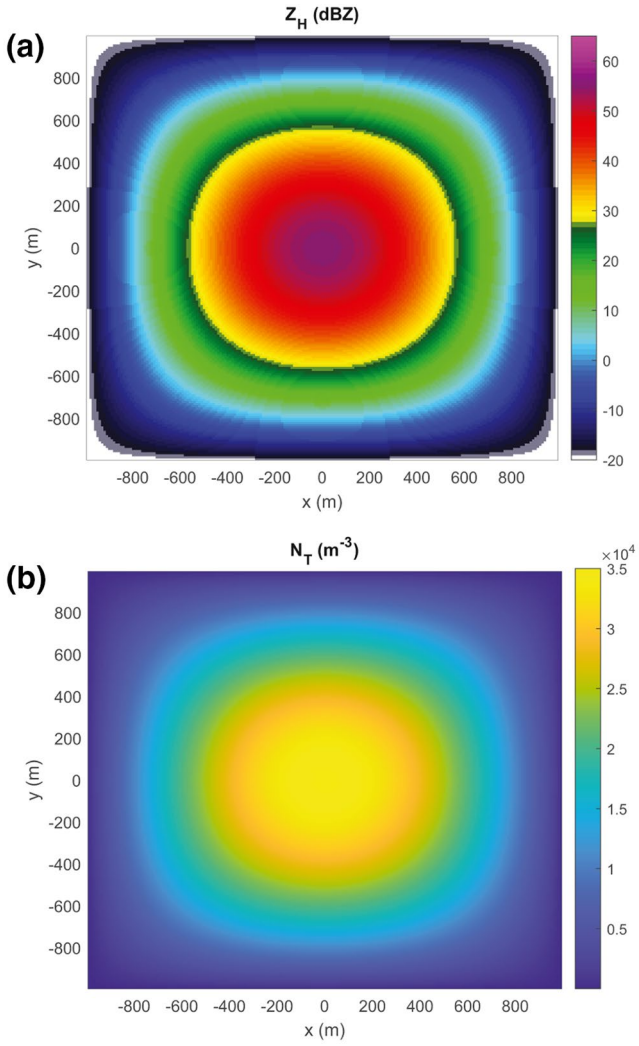

Figure 2. (a) Z_H (dBZ) and (b) N_T (m^{-3}) values prescribed at the top of model domain.

where $u(z)$ and $v(z)$ are the x- and y-components of the horizontal wind at a given height z and $v_t(D)$ is the fall speed for a drop with a diameter equal to D. $N(D)$ is the number concentration for drops with diameter D. A 2-km wide raindrop generating "cloud base" is initialized at the upper boundary of the domain centered at (0 km and 0 km). Although we choose a single level for producing raindrops for simplicity, in reality different sized raindrops will be produced at several different levels, especially for deep convective systems. The center of the cloud is given a Z_H value of 55 dBZ and a total number concentration (N_T) of 35,000 m^{-3}. Both of these values decrease sinusoidally toward the edges of the cloud to −20 dBZ and 0 m^{-3}, respectively (Figure 2).

We then use the Z_H and N_T values for each grid in the cloud base and assume a three-parameter gamma distribution,

$$N(D) = N_0 D^{\mu} e^{-\Lambda D}, \tag{2}$$

to get the initial DSD at the top of the domain. In Equation 2 N_0, Λ, and μ are the intercept, slope, and shape parameters, respectively, and we assume a shape parameter of $\mu = 1$ for our experiments. Raindrops are divided into 41 size bins (0.1–8.1 mm in 0.2-mm intervals). The DSDs for each grid box are converted into polarimetric variables at S band using the forward operator described in Ryzhkov et al. (2011), K12, and Kumjian and Prat (2014). We assume the raindrops are pure liquid water at 20°C, and are oriented with a mean canting angle with respect to vertical of 0° with a standard deviation of the distribution of canting angles of 10°. All grids with $Z_H < -20$ dBZ are filtered out for all variables. The domain is 3 km tall. Grid spacing is 50 m in the vertical and 10 m in the horizontal. For the terminal fall speeds of different raindrop size bins, we use the equation relating fall speed v_t (m s^{-1}) and drop size D (mm) given in Brandes et al. (2002) and shown in Equation 3, due to the excellent agreement with observations (e.g., Thurai & Bringi, 2005).

$$v_t = -0.1021 + 4.932D - 0.9551D^2 + 0.07934D^3 - 0.002362D^4 \tag{3}$$

While this equation represents pure sedimentation, in reality raindrops quite often fall in the presence of downdrafts. For stronger downdrafts, the results may change more noticeably but even for downdrafts on the order of a few m s^{-1} the differences are small (not shown).

2.2. Wind Fields

Several different types of vertical profiles of storm-relative wind are used in these experiments (Figure 3). Some of these wind profiles only contain a u-component (i.e., $v = 0$ at all heights). One such profile is the "linear" wind profile, where the storm-relative winds (easterlies, in this case) increase linearly moving downward from 0 m s^{-1} at the top of the domain to magnitudes near the surface varying between 5 and 30 m s^{-1} (Figure 3a). Another profile is the "exponential" wind profile, where the storm-relative winds have an exponential dependence on height,

$$u(z) = u_{\text{sfc}} \left(\frac{z_{\text{top}} - z}{z_{\text{top}}} \right)^a \tag{4}$$

where u_{sfc} is the wind near the surface and z_{top} is the height of the domain top. For these wind profiles, $u = 0$ m s^{-1} at the top of the domain and $u = -20$ m s^{-1} at the bottom, giving a shear value of 20 m s^{-1} over

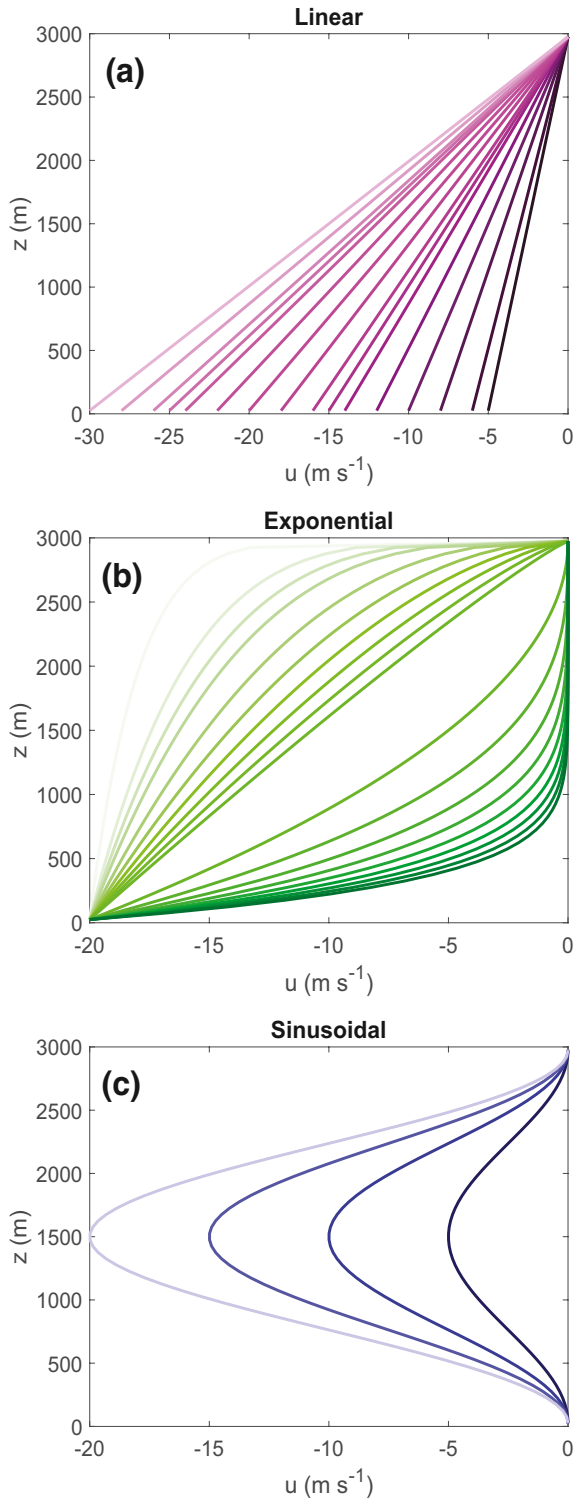

Figure 3. The (a) linear, (b) exponential, and (c) sinusoidal "u-only" storm-relative wind profiles. Darker (lighter) shading indicates a weaker (stronger) mean storm-relative wind.

the entire layer. However, the exponent a determines where a majority of the shear is distributed, with $a > 1$ concentrating shear in the lower levels of the domain, $a < 1$ concentrating shear in the upper levels, and $a = 1$ gives the linear profile. We vary a from 0.1 to 10 (Figure 3b). The reason for including these profiles is to assess the different size sorting effects from profiles with the same amount of bulk shear but concentrated in different layers which leads to different storm-relative wind profiles.

An additional "u-only" profile used in this study is the "sinusoidal" wind profile. For these wind profiles, there is a sinusoidal dependence of u with height such that the storm-relative winds are $u = 0$ m s^{-1} at both the top and bottom of the domain (i.e., shear is 0 m s^{-1}) with a peak of varying magnitudes halfway in between. The sinusoidal peaks are varied between 5 and 20 m s^{-1} (Figure 3c). Much like the exponential profiles, we use the sinusoidal profiles to illustrate the different size sorting effects from profiles with the same amount of bulk shear. The sinusoidal profiles are a unique case because they have zero bulk shear but still contain nonzero storm-relative winds.

We also use several wind profiles where both u and v vary as a function of height (Figure 4). One is a quarter-circle turn in the bottom half of the domain and one-dimensional shear in the u direction in the top half of the domain, similar to hodographs used in previous modeling work (e.g., Rotunno & Klemp, 1982). The radius of the quarter-circle turn and the magnitude of unidirectional shear in the u direction both vary between 10 and 20 m s^{-1}. The quarter-circle turn hodograph is centered around the origin (0 m s^{-1}, 0 m s^{-1}) in a storm-relative frame of reference (Figure 4, magenta line). We also use half-circle hodographs with radii varying between 10 and 20 m s^{-1} and centered around various points between -2 and 2 m s^{-1} for both u and v (Figure 4, black line). Half-circle hodographs represent flows with mostly streamwise vorticity and have been used in modeling studies of convective weather (e.g., Markowski & Richardson, 2014; Weisman & Klemp, 1984). Lastly, we use three different observed soundings from Norman, OK (OUN), at 00Z on May 9, 2003 and 18Z on May 20, 2013, and from Birmingham, AL (BMX), at 18Z on April 27, 2011 (Figure 4, yellow, maroon, and blue lines). These three soundings were chosen because they were associated with significantly tornadic supercells and provide more realistic variability compared to the idealized wind profiles. Storm motions for the three observed soundings were randomly chosen within 10 m s^{-1} of the storm motion calculated for right-moving supercells from the method in Bunkers et al. (2000).

3. Results

3.1. Z_{DR} and K_{DP} Magnitude/Separation and Storm-Relative Winds

We employ the simple model described in the previous section to assess the relationship between the Z_{DR} and K_{DP} fields and the storm-relative winds. We compare the magnitude (or maximum values) of the Z_{DR} and K_{DP} fields with the magnitude of the mean storm-relative wind (Figure 5). Specifically, we look at the maximum values at the bottom of the layer after all size sorting has occurred. The maximum Z_{DR} value exhibits a clear relationship with the mean storm-relative wind magnitude, where stronger storm-relative winds are associated with greater maximum Z_{DR}. As the storm-relative wind magnitudes increase, they are able to advect

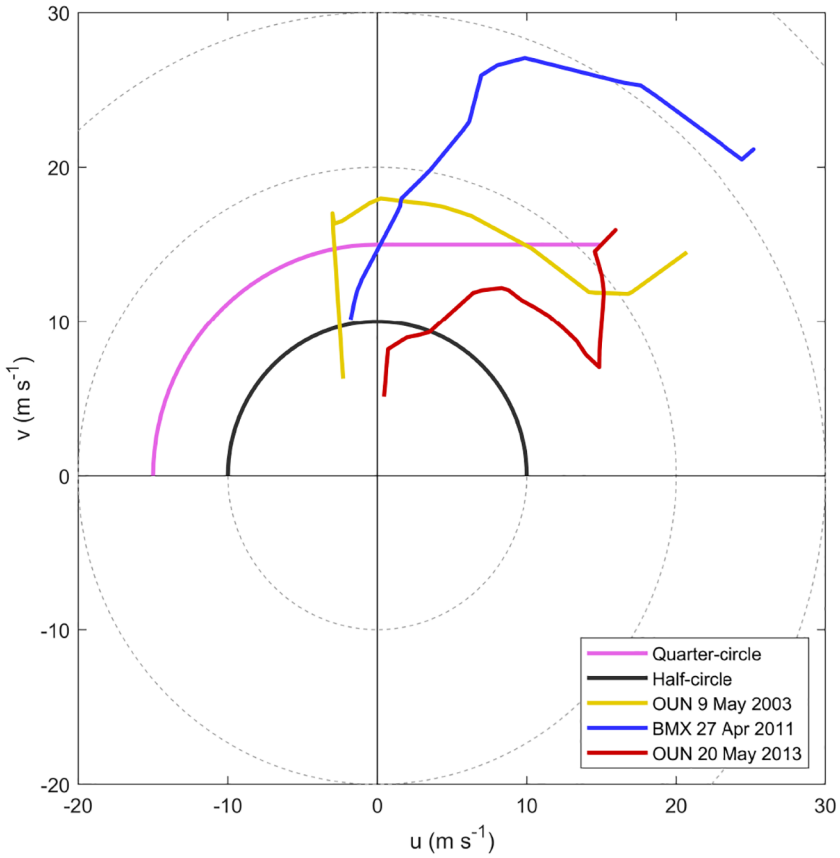

Figure 4. Examples of the five hodographs used. The quarter-circle (magenta) and half-circle (black) hodographs shown are storm-relative (i.e., storm motion at [0 m s^{-1}, 0 m s^{-1}]) while the three observed hodographs are ground-relative.

not only smaller drops, but progressively larger drops further downstream so that what is left upstream are fewer drops with increasing drop size, leading to an increase in Z_{DR}.

The maximum K_{DP} at the bottom of the sorting layer exhibits the opposite relationship: as the mean storm-relative wind increases the maximum K_{DP} value decreases. With increasing storm-relative winds, the initial concentration and mass of drops disperses more, which decreases the number concentration and liquid mass. Because K_{DP} is sensitive to number concentration and liquid mass, this leads to a decrease in K_{DP}. Unlike in the plot of Z_{DR} and mean storm-relative wind, there is a separation between the "*u*-only" wind profiles and the wind profiles where both *u* and *v* vary with height for K_{DP} maxima. The "*u*-only" wind profile cases are able to maintain slightly larger maximum K_{DP} values because the drops are only being spread out in one direction owing to the wind profiles only containing easterly winds. The wind profiles where both *u* and *v* vary with height allow the drops to be dispersed in any direction, leading to a further reduction in number concentration and, therefore, K_{DP}.

In addition to the Z_{DR} and K_{DP} maxima, we also use the simple model to assess the separation between these maxima and how it relates to the storm-relative winds. D15 used the distance between a smaller 0.5 mm drop and a larger 8 mm drop after they had fallen through a layer to analyze the degree of size sorting. Our approach of using the distance between Z_{DR} and K_{DP} maxima is similar, assuming that a maximum in Z_{DR} signals a sparse concentration of larger drops and a maximum in K_{DP} signals a large concentration of relatively smaller drops. However, our approach is more applicable to observations than the separation of 0.5 mm and 8 mm drops. Whereas using point max values with operational radar data is susceptible to noise, it is acceptable to do so in this idealized model framework because we are not concerned with Z_{DR} biases (Cunningham et al. 2013; Zittel et al., 2014), K_{DP} censoring, and other operational issues that can

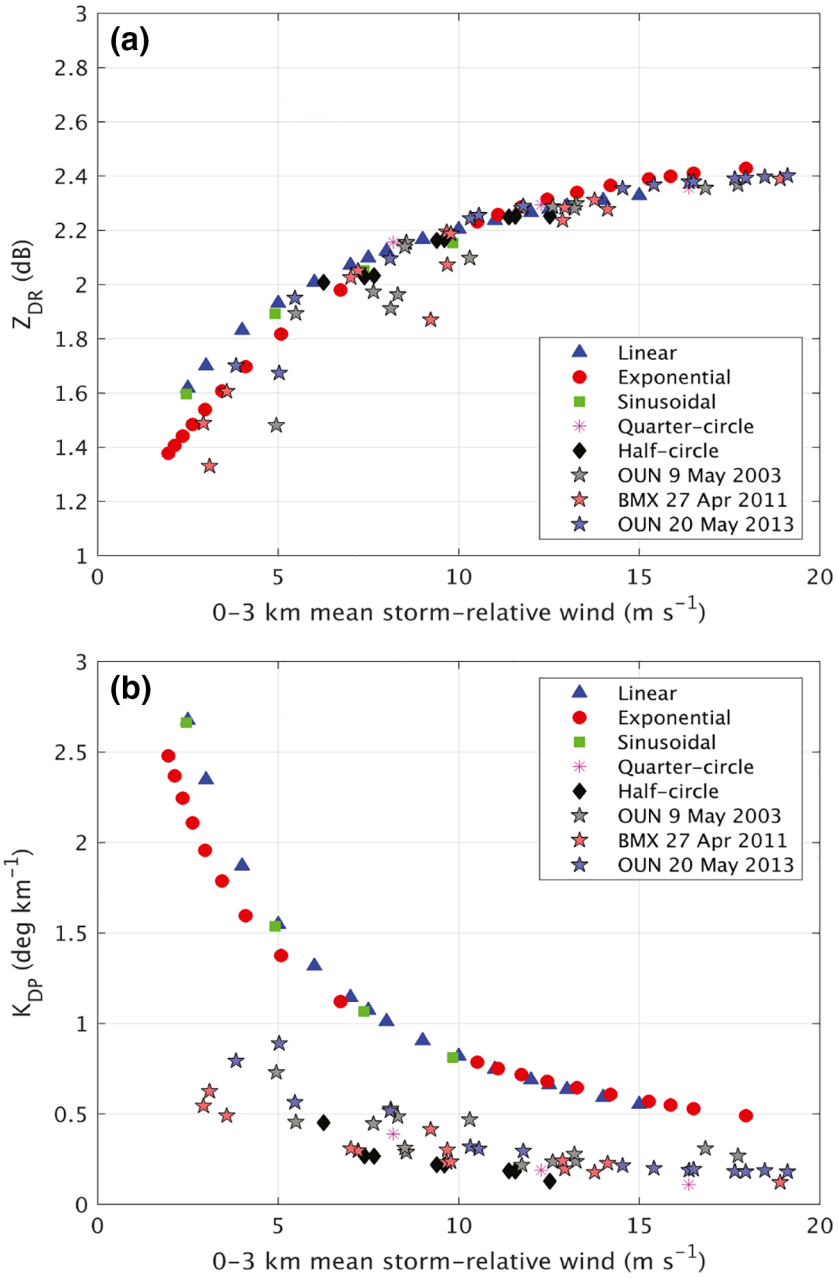

Figure 5. (a) Maximum Z_{DR} (dB) at the bottom of the domain compared to the magnitude of the mean storm-relative wind over the sorting layer (m s^{-1}). Linear (blue triangles), exponential (red circles), sinusoidal (green squares), quarter-circle (magenta asterisks), half-circle (black diamonds), and the three observed soundings (varying colored pentagrams) are all represented. (b) Same as in (a) only comparing maximum K_{DP} (deg km^{-1}) at the bottom of the domain with the mean storm-relative wind magnitude.

affect the radar variables. Measurement errors in Z_{DR} can be a few tenths of a dB (Cunningham et al., 2013), whereas K_{DP} uncertainty typically is taken to be about 0.1–0.2 deg km^{-1} at S band (e.g., Ryzhkov et al., 2005). Further, regions of enhanced K_{DP} can be censored out if they have reduced values of co-polar correlation coefficient. As such, we have advocated for using an area-based approach for identifying low-level Z_{DR} and K_{DP} enhancement regions in observations (Loeffler & Kumjian, 2018; Loeffler et al., 2020). Loeffler and Kumjian (2018) identified two components of this Z_{DR}–K_{DP} separation which comprised their "separation vector": the distance and orientation of separation. In their study, this vector pointed from the K_{DP} maximum toward the Z_{DR} maxima, which is, theoretically, directed from smaller toward larger drops. In

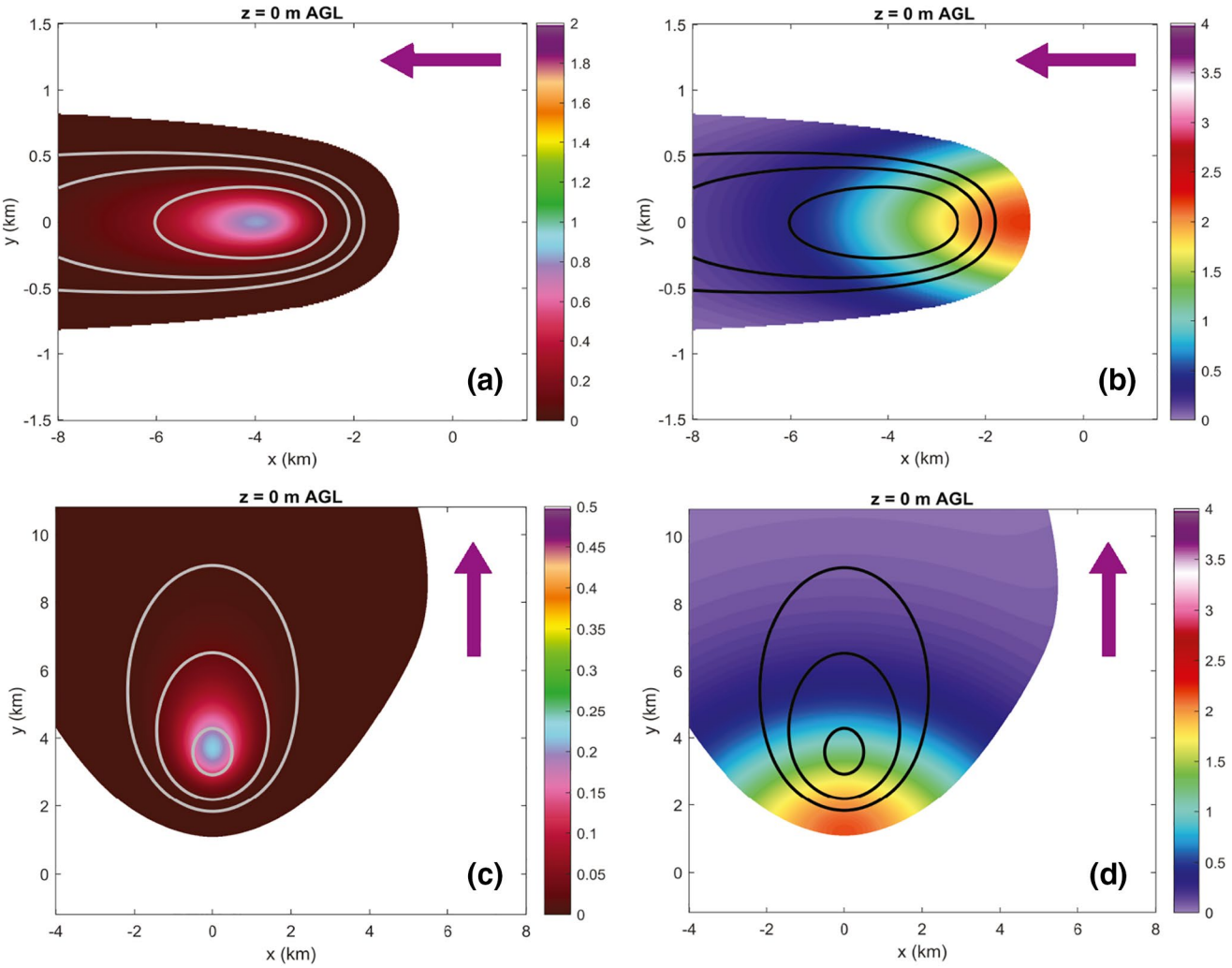

Figure 6. (a) K_{DP} (deg km^{-1}, shaded) and (b) Z_{DR} (dB, shaded) at the bottom of the layer for a linear case with 20 m s^{-1} of shear. (c) and (d) Similar to (a) and (b) but for a half-circle case with a radius of 15 m s^{-1}. Z_H contours at 20, 30, and 40 dBZ are overlaid. The mean storm-relative wind direction is indicated in each panel in the upper right-hand corner (purple arrows).

this study, the orientation of separation is directed from the Z_{DR} maximum toward the K_{DP} maximum to be theoretically aligned from larger to smaller drops and therefore with the mean storm-relative wind as well. This is similar to past works (e.g., D15) that looked at the direction of decreasing Z_{DR}, which also would be directed from larger to smaller drops.

We assess the Z_{DR}–K_{DP} separation by analyzing the polarimetric fields at the bottom of the layer, shown in Figure 6. The top row of Figure 6 shows these fields for a linear case with 20 m s^{-1} of shear and the bottom row shows a case with a half-circle hodograph with a radius of 15 m s^{-1}. For the linear case the mean storm-relative wind is easterly, whereas the half-circle case has a southerly mean storm-relative wind. For both cases, the K_{DP} maximum is co-located (or very nearly co-located) with the Z_H maximum and the Z_{DR} maximum is located toward the upwind side of the precipitation field. Additionally, the orientation of the separation from the Z_{DR} to K_{DP} maximum is aligned with the mean storm-relative wind.

We perform this type of analysis for each wind profile experiment. D15 illustrated that the storm-relative winds are the fundamental mechanism responsible for size sorting, not vertical wind shear or SRH as suggested by Kumjian and Ryzhkov (2009). Figures 7 and 8 illustrate this point. Figure 7 shows the lack of the correlation between the shear in a layer and the separation distance of Z_{DR} and K_{DP} maxima, owing to shear being determined by the storm-relative wind vectors solely at the upper and lower boundaries of the

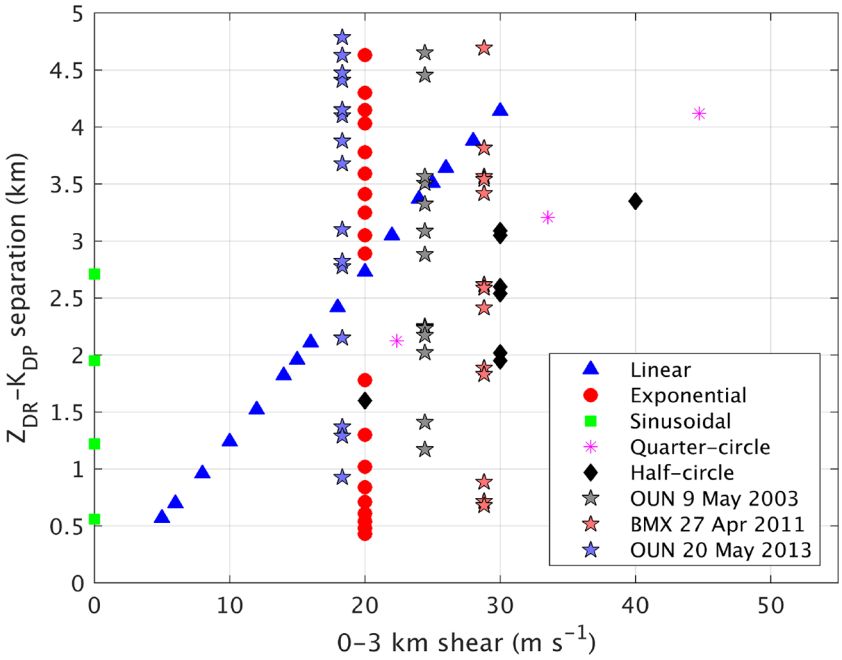

Figure 7. Comparison of the separation distance (km) between Z_{DR} and K_{DP} maxima and the shear in the layer (m s^{-1}). Symbols are the same as in Figure 5.

domain, while the winds throughout the layer are fundamental for size sorting. For the linear cases, there is a clear relationship because the wind speed values at the upper and lower boundaries directly influence the storm-relative wind profile. However, one shear value can produce several different degrees of size sorting as evident by the exponential, sinusoidal, and the three observed soundings. All of the exponential wind profiles have the same shear value, but profiles with shear concentrated in the lower levels have weaker

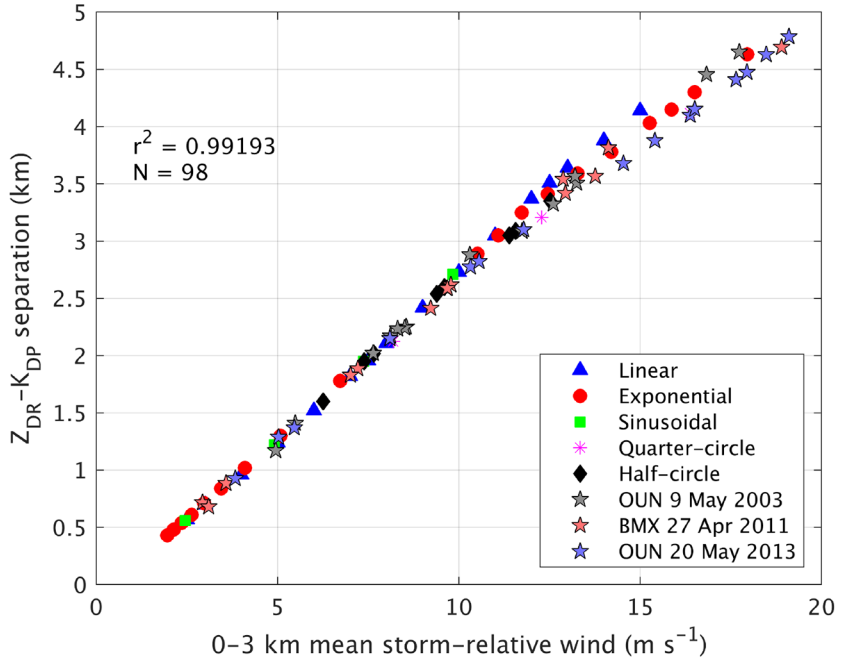

Figure 8. Comparison of the separation distance (km) between Z_{DR} and K_{DP} maxima and the mean storm-relative wind magnitude (m s^{-1}). Symbols are the same as in Figure 5.

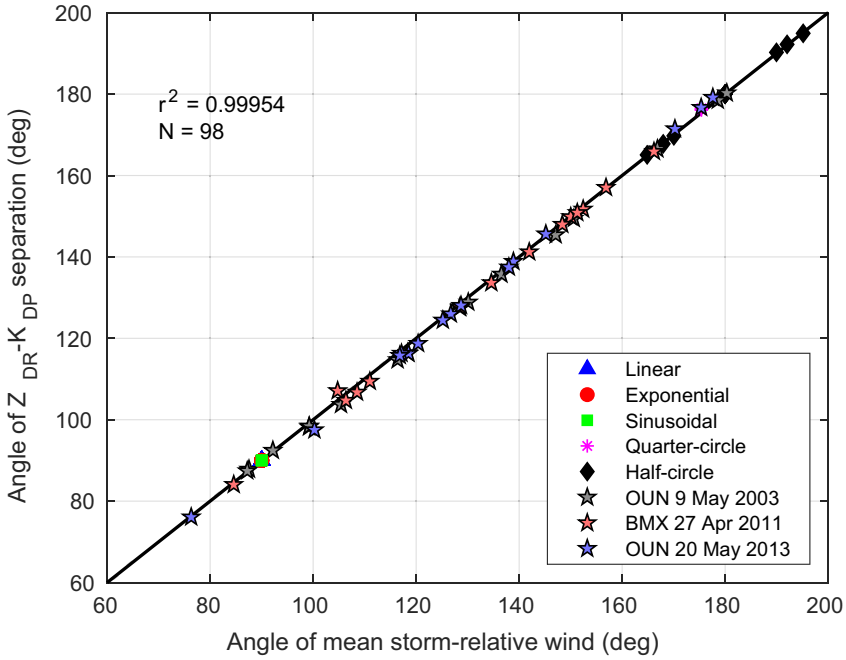

Figure 9. Angle of separation orientation from the Z_{DR} to the K_{DP} maximum compared with the mean storm-relative wind angle. Symbols are the same as in Figure 5.

mean storm-relative winds and therefore less size sorting compared to those with shear concentrated in the upper levels. The sinusoidal profiles have zero shear but nonzero storm-relative flow. An increased peak in the wind profile increases the storm-relative winds and therefore the degree of size sorting as well. The three observed soundings will keep the same shear values regardless of the storm motion, whereas the storm-relative winds will change with varying storm motions. On the other hand, Figure 8 shows a clear relationship ($r^2 = 0.992$) between the magnitude of the mean storm-relative wind and the Z_{DR}–K_{DP} separation distance measured at the bottom of the layer.

In addition to the separation distance, the separation orientation is also analyzed. We expect the separation orientation from Z_{DR} to K_{DP} to be aligned with the mean storm-relative wind, as is shown in Figure 6. This is confirmed in Figure 9. There is a large clustering of points at (90°, 90°) from the "u-only" cases (linear, exponential, and sinusoidal) because they contain only easterly winds throughout the layer. However, the relationship holds for the wind profiles where both u and v vary with height with $r^2 = 0.999$ for all wind profiles. The 1:1 line is plotted for reference and shows that the angle of separation from Z_{DR} to K_{DP} is very close, if not identical, to the mean storm-relative wind orientation.

3.2. Z_{DR}–K_{DP} Separation and SRH

In an effort to link the two components of separation discussed by Loeffler and Kumjian (2018) to characteristics of the wind field, specifically SRH, those authors created a "size sorting parameter." The size sorting parameter (SSP) was defined as SSP = $D_{sep} \times \sin|A|$, where D_{sep} was the separation distance and A was the angle of the K_{DP} to Z_{DR} separation taken clockwise from the storm motion vector. In their study, A could be negative (hence the absolute value) but in our study all the orientation angles are positive. For this study, we define A_{shr} as the angle of the Z_{DR} to K_{DP} separation taken counter-clockwise from the shear vector in the layer, and use A_{shr} in place of A for calculating SSP. The SSP increases for increasing separation distance and separation angles that are increasingly orthogonal to the shear vector. This is because of the strong relationship between separation distance and orientation with the mean storm-relative wind magnitude and orientation, respectively (Figures 8 and 9). Additionally, a larger mean storm-relative wind that is oriented more orthogonal to the shear vector sweeps out more area under the hodograph and therefore is associated with increased SRH.

To assess how each component, distance or orientation, impacts the SSP and is related to SRH, we run simulations where either the separation distance or orientation is kept constant while the other is varied. For these experiments, we use the three observed soundings and vary storm motions such that only distance or orientation is held constant. This is depicted in Figure 10, with the yellow marker showing the mean ground-relative wind and the other varying colored markers showing the different storm motions. The mean storm-relative wind is directed from the tip of the storm motion vector to the tip of the mean ground-relative wind vector. The left column shows the different storm motions for the three soundings that produce similar separation orientation angles but varying separation distances while the right column shows the storm motions that produce similar distances with varying separation orientations.

The results of the simulations using the wind profiles from Figure 10 are shown in Figure 11. The top row depicts the relationship between separation distance and the SRH in the layer. We can see a clear relationship between distance and SRH (Figure 11a) for each sounding when only distance is varied (i.e., orientation held constant), where increasing separation distances correlate to higher values of SRH. However, when orientation is varied and distance held constant we still see a variety of SRH values for a given separation distance (Figure 11b), illustrating that separation distance cannot be the only factor in estimating SRH from Z_{DR}−K_{DP} separation.

The middle row compares separation orientation and SRH. Once again, there is a clear relationship for each sounding between orientation and SRH when only orientation angles are varied and distances held constant (Figure 11d), where SRH is maximized for orientation angles close to 90° (i.e., orthogonal to the shear vector). On the other hand, we can see that there is still variability of SRH values among similar orientation values when separation distances vary (Figure 11c), illustrating that separation orientation also cannot be the only factor in estimating SRH. The top two rows illustrate that for a certain distance, SRH tends to increase for more orthogonal orientations and that for a certain orientation, SRH tends to increase with increasing distance, in agreement with arguments from Loeffler and Kumjian (2018). The variation of SRH values for a given sounding is larger when varying the separation distance as compared to varying the separation orientation, implying that separation distance perhaps has a stronger relationship with SRH than orientation.

The SSP is shown on the bottom row of Figure 11. In this case, there is an obvious relationship ($r^2 > 0.98$) for each sounding between the SSP and SRH, regardless of whether separation distance or orientation is varied. The bottom row shows that for a given sounding, increasing SSP is associated with increased SRH. The variability of SRH between the different soundings is due to the differences in the area between the ground-relative mean wind (yellow markers in Figure 10) and the hodograph.

In addition to the simulations where either separation distance or orientation is held constant, we perform the same analysis on the simulations with random storm motions discussed in Section 2. The results are shown in Figure 12. The top row of the figure shows a positive relationship, although not as strong as in Figure 11, for a given sounding between separation distance and SRH even when orientation values vary. This is in agreement with D15 and their correlation between the hydrometeor size sorting magnitude and SRH. The middle row shows the comparison between orientation and SRH. Whereas it was a clear relationship when separation distance was held constant (Figure 11d), it is difficult to discern such a relationship between orientation and SRH when separation distance is also varying. This points to the separation distance having a stronger relationship with SRH than the orientation does. The bottom row depicts the relationship between SSP and SRH. Once again, for each sounding SSP shows a strong relationship ($r^2 > 0.99$) with SRH, signaling that taking into account both separation distance and orientation improves the estimation of SRH compared to using just one.

4. Conclusions and Future Work

This study utilizes a simple model to assess the relationship between the storm-relative winds and the K_{DP} and Z_{DR} fields. For the first time, we are able to isolate the effects of storm-relative winds and SRH on the separation distance and orientation between regions of enhanced Z_{DR} and K_{DP} values. Previous studies have demonstrated that the fundamental process for hydrometeor size sorting as well as the effects of size sorting on the polarimetric radar variables is the presence of storm-relative winds. Recent observational work has

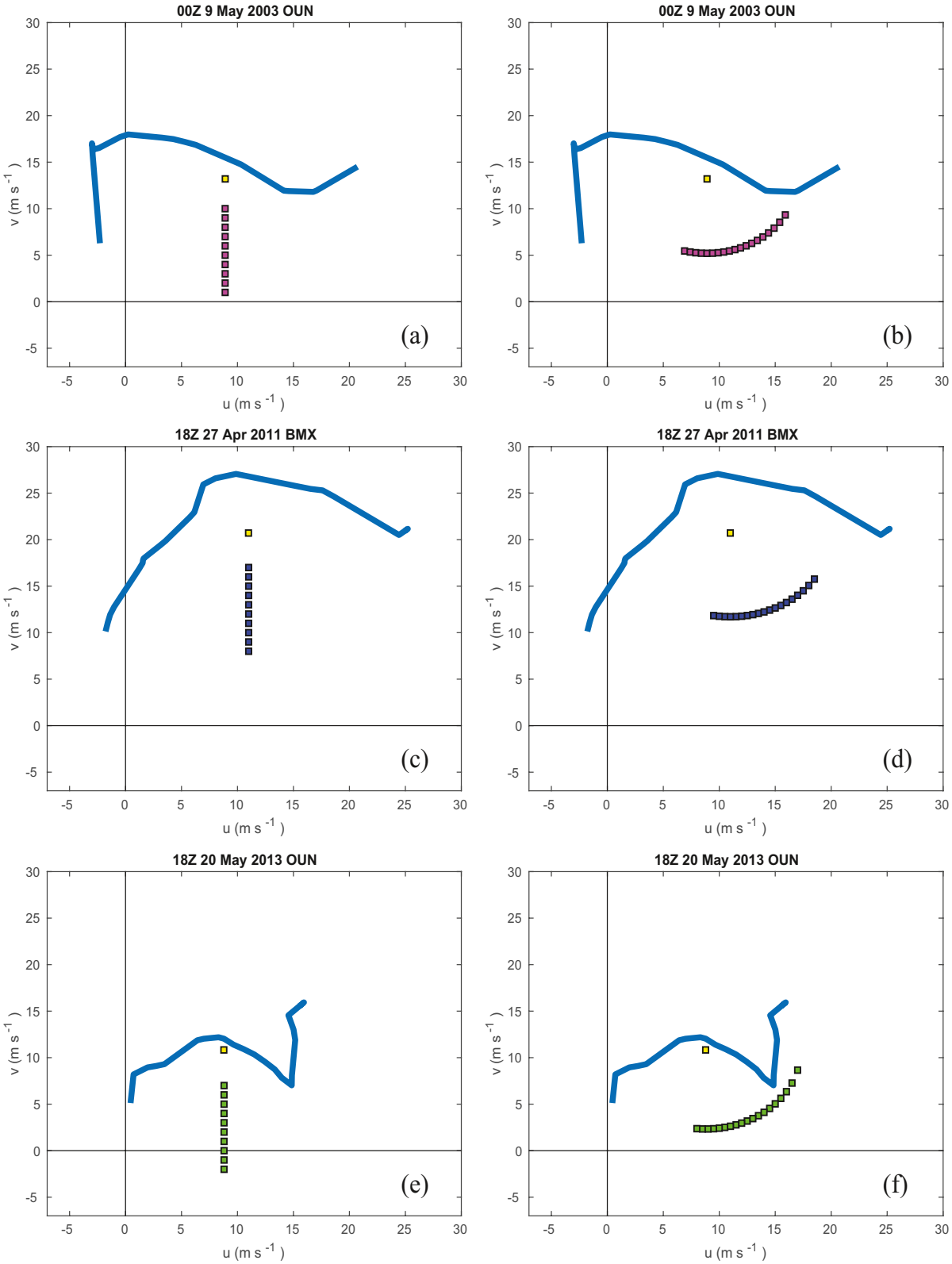

Figure 10. (a) Hodograph from 00Z May 9, 2003 (OUN) with mean ground-relative wind (yellow square) and varying storm motions (magneta squares) producing similar separation orientations but varying distances. (b) Same as (a) except for producing similar separation distances but varying orientations. (c) and (d) Similar to (a) and (b) except for 18Z April 27, 2011 (BMX) with storm motions in blue. (e) and (f) Same as (a) and (b) except for 18Z May 20, 2013 (OUN) with storm motions in green.

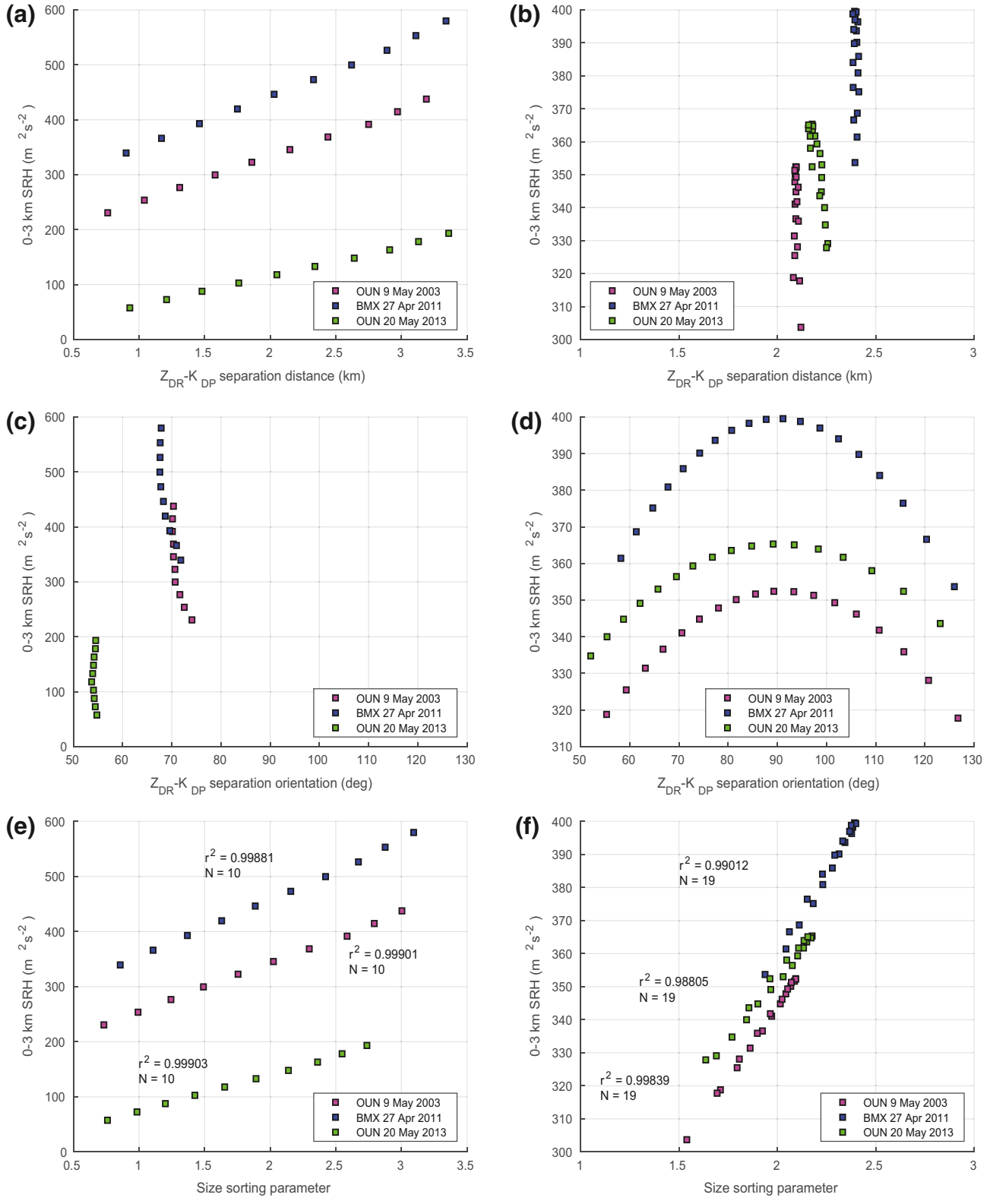

Figure 11. (a) 0–3 km SRH ($m^2 s^{-2}$) compared with separation distance while orientation angle is held constant. (b) Same as (a) but for separation distance being held constant. (c) and (d) Similar to (a) and (b) except for separation orientation. (e) and (f) Same as (a) and (b) except for the size sorting parameter. The left column shows simulations with similar separation orientations but varying distances, and the right column shows simulations with similar separation distances but varying orientations. Same corresponding sounding markers used as in Figure 10.

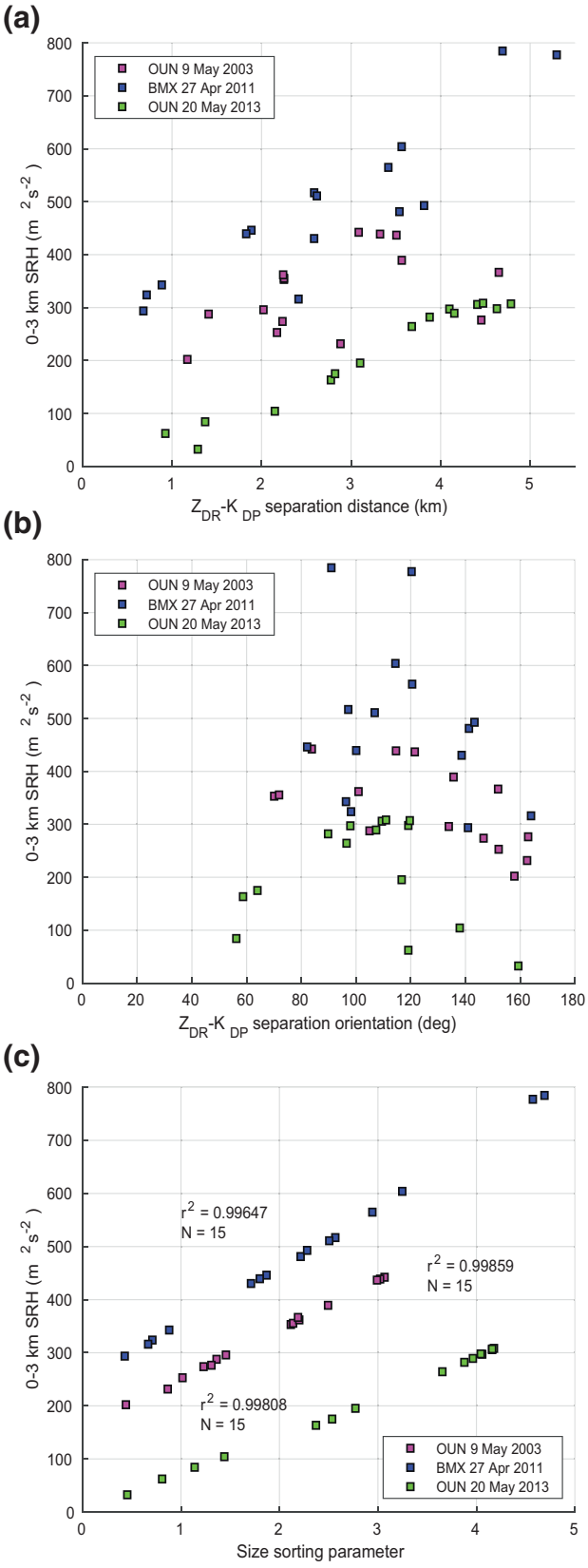

Figure 12. Similar to Figure 11 except for random storm motions. 0-3 km SRH compared to (a) separation distance, (b) separation orientation, and (c) size sorting parameter.

attempted to link the enhanced regions of K_{DP} and Z_{DR}, both in separation distance and orientation, in convective storms to the storm-relative wind profile and SRH in the near-storm environment.

The 3-D numerical model used in this study is very simplified as only rain is considered (i.e., no frozen or melting precipitation) and we ignore microphysical processes such as evaporation, breakup, and coalescence. Only sedimentation and horizontal advection are considered in the model. Therefore, the results in this study are only valid for the sorting of raindrops. In reality, raindrops usually fall in the presence of downdrafts and not just pure sedimentation by gravity. However, a downdraft would simply add the same magnitude to the fall speed across all drop sizes, leading to the same fundamental result that large drops fall through a layer faster than smaller drops. Therefore, we believe the results presented here are still valid when downdrafts are considered. The presence of an updraft could perhaps be a bit more complicated, as it could enhance size sorting by completely removing smaller drops from participating in the fallout, for example, Kumjian and Ryzhkov (2012). However, if a sufficiently broad spectrum of drop sizes was able to fall out against the updraft such that medium-sized drops were present in relatively larger concentrations (contributing to increased K_{DP}) and larger drops present in relatively lower concentrations (contributing to increased Z_{DR}), we would still expect to see qualitatively similar separation of enhanced Z_{DR} and K_{DP} regions. We apply several idealized wind profiles where both u and v can vary with height as well some observed profiles for use in the model. The polarimetric radar variables are then calculated from the resulting DSD's throughout the domain and we assess the K_{DP} and Z_{DR} fields at the bottom of the domain.

The analysis of the K_{DP} and Z_{DR} fields at the bottom of the domain shows that the Z_{DR} field magnitude increases with increasing mean storm-relative wind magnitude, whereas the K_{DP} field magnitude decreases with increasing mean storm-relative wind magnitude. Increasing storm-relative winds lead to increased size sorting which increases the median drop size upwind, increasing Z_{DR}, and reduces the number concentration, decreasing K_{DP}. Further, we assess the separation between the K_{DP} and Z_{DR} maxima at the bottom of the domain for both distance and orientation. The separation distance has little correlation with the shear in the layer as several different magnitudes of the mean storm-relative wind, and therefore size sorting, can be associated with a single shear value. However, there is a strong correlation between the mean storm-relative wind magnitude and the Z_{DR}–K_{DP} separation distance. Additionally, the orientation of separation from Z_{DR} to K_{DP} is aligned with the mean storm-relative wind.

In order to assess how the separation distance and/or orientation are related to the SRH in the layer, we perform simulations where either distance or orientation is held constant while the other one varies. For a given orientation, increasing SRH is associated with increasing distance. For a certain distance, increasing SRH is associated with orientations more orthogonal to the shear vector in the layer. For random storm motions, separation distance tends to have a stronger correlation with SRH than does orientation. However, the SSP has a strong correlation with SRH regardless of whether separation distance, orientation, or both are varied.

Further understanding of the relationship between the polarimetric fields and storm-relative winds is important for utilizing radar data to gain insight into the dynamics of convective storms. Further observational work would be beneficial to add to the theoretical framework and results presented in this study. Additionally, future work will assess these size sorting signatures in a more sophisticated numerical modeling framework (i.e., full cloud model) in order to gain further insight into their relationship with the storm dynamics and microphysical processes.

Data Availability Statement

Model scripts and input files are available through the Penn State Data Commons (https://doi.org/10.26208/rvmz-ks26).

Acknowledgments
The authors thank the members of the Penn State RADAR group for their helpful comments and suggestions throughout this work. We also thank three anonymous reviewers for their constructive feedback on an earlier version of this manuscript. This work was funded by the VORTEX-SE program under Award NA19OAR4590222.

References

Beard, K. V. (1976). Terminal velocity and shape of cloud and precipitation drops aloft. *Journal of the Atmospheric Sciences*, *33*, 851–864.

Benjamin, S. G., Weygandt, S. S., Brown, J.M., Hu, M., Alexander, C.R., Smirnova, T.G., et al. (2016). A North American hourly assimilation and model forecast cycle: The Rapid Refresh. Monthly *Weather Review, 144,* 1669–1694. https://doi.org/10.1175/MWR-D-15-0242.1466 Brandes, E. A., Zhang, G., & Vivekanandan, J. (2002). Experiments in rainfall estimation with a polarimetric radar in a subtropical environment. *Journal of Applied Meteorology*, *41*, 674–685. https://doi.org/10.1175/1520-0450(2002)041<0674:EIREWA>2.0.CO;2

Bunkers, M. J., Klimowski, B. A., Zeitler, J. W., Thompson, R. L., & Weisman, M. L. (2000). Predicting supercell motion using a new hodograph technique. *Weather and Forecasting*, *15*, 61–79. https://doi.org/10.1175/1520-0434(2000)015<0061:PSMUAN>2.0.CO;2

Crowe, C. C., Schultz, C. J., Kumjian, M., Carey, L. D., & Petersen, W. A. (2012). Use of dual-polarization signatures in diagnosing tornadic potential. *Electronic Journal of Operational Meteorology*, *13*, 57–78.

Cunningham, J. G., Zittel, W. D., Lee, R. R., Ice, R. L., & Hoban, N. P. (2013). *Methods for identifying systematic differential reflectivity (ZDR) biases on the operation WSR-88D network*. Paper presented at the 36th Conference on Radar Meteorology. American Meteorological Society, Breckenridge, CO.

Dawson, D. T., Mansell, E. R., Jung, Y., Wicker, L. J., Kumjian, M. R., & Xue, M. (2014). Low-level Z_{DR} signatures in supercell forward flanks: The role of size sorting and melting of hail. *Journal of the Atmospheric Sciences*, *71*, 276–299. https://doi.org/10.1175/JAS-D-13-0118.1

Dawson, D. T., Mansell, E. R., & Kumjian, M. R. (2015). Does wind shear cause hydrometeor size sorting?. *Journal of the Atmospheric Sciences*, *72*, 340–348. https://doi.org/10.1175/JAS-D-14-0084.1

Foote, G. B., & du Toit, P. S. (1969). Terminal velocity of raindrops aloft. *Journal of Applied Meteorology*, *8*, 249–253.

Gunn, R., & Kinzer, G. D. (1949). The terminal velocity of fall for water droplets in stagnant air. *Journal of Meteorology*, *6*, 243–248.

Gunn, K., & Marshall, J. (1955). The effect of wind shear on falling precipitation. *Journal of Meteorology*, *12*, 339–349.

Jurewicz, M., & Gitro, C. (2014). *The utility of considering dual-polarization radar signatures in the tornado warning process.* 22nd U.S./Canada Great Lakes Operational Meteorology Workshop. National Weather Association, Ann Arbor, MI.

Kingfield, D., & Picca, J. (2018). Development of an operational convective nowcasting algorithm using raindrop size sorting information from polarimetric radar data. *Weather and Forecasting*, *33*, 1477–1495.

Kumjian, M. R. (2013). Principles and applications of dual-polarization weather radar. Part I: Description of the polarimetric radar variables. *Journal of Operational Meteorology*, *1*, 226–242. https://doi.org/10.15191/nwajom.20130119

Kumjian, M. R., Lebo, Z. J., & Morrison, H. C. (2015). On the mechanisms of rain formation in an idealized supercell storm. *Monthly Weather Review*, *143*, 2754–2773. https://doi.org/10.1175/MWR-D-14-00402.1

Kumjian, M. R., Martinkus, C. P., Prat, O. P., Collis, S., van Lier-Walqui, M., & Morrison, H. C. (2019). A moment-based polarimetric radar forward operator for warm rain microphysics. *Journal of Applied Meteorology and Climatology*, *58*, 113–130.

Kumjian, M. R., & Prat, O. P. (2014). The impact of raindrop collisional processes on the polarimetric radar variables. *Journal of the Atmospheric Sciences*, *71*, 3052–3067. https://doi.org/10.1175/JAS-D-13-0357.1

Kumjian, M. R., & Ryzhkov, A. V. (2008). Polarimetric signatures in supercell thunderstorms. *Journal of Applied Meteorology and Climatology*, *47*, 1940–1961. https://doi.org/10.1175/2007JAMC1874.1

Kumjian, M. R., & Ryzhkov, A. V. (2009). Storm-relative helicity revealed from polarimetric radar measurements. *Journal of the Atmospheric Sciences*, *66*, 667–685. https://doi.org/10.1175/2008JAS2815.1

Kumjian, M. R., & Ryzhkov, A. V. (2012). The impact of size sorting on the polarimetric radar variables. *Journal of the Atmospheric Sciences*, *69*, 2042–2060. https://doi.org/10.1175/JAS-D-11-0125.1

Laurencin, C. N., Didlake, A. C., Loeffler, S. D., Kumjian, M. R., & Heymsfield, G. M. (2020). Hydrometeor size sorting in the asymmetric eyewall of hurricane Matthew (2016). *Journal of Geophysical Research*, *125*, e2020JD032671. https://doi.org/10.1029/2020JD032671

Loeffler, S. D., & Kumjian, M. R. (2018). Quantifying the separation of enhanced Z_{DR} and K_{DP} regions in nonsupercell tornadic storms. *Weather and Forecasting*, *33*, 1143–1157.

Loeffler, S. D., Kumjian, M. R., Jurewicz, M., & French, M. M. (2020). Differentiating between tornadic and nontornadic supercells using polarimetric radar signatures of hydrometeor size sorting. *Geophysical Research Letters*, *47*, e2020GL088242. https://doi.org/10.1029/2020GL088242

Markowski, P., & Richardson, Y. P. (2014). The influence of environmental low-level shear and cold pools on tornadogenesis: Insights from idealized simulations. *Journal of the Atmospheric Sciences*, *71*, 243–275. https://doi.org/10.1175/JAS-D-13-0159.1

Marshall, J. (1953). Precipitation trajectories and patterns. *Journal of Meteorology*, *10*, 25–29.

Martinaitis, S. M. (2017). Radar observations of tornado-warned convection associated with tropical cyclones over Florida. *Weather and Forecasting*, *32*, 165–186. https://doi.org/10.1175/WAF-D-16-0105.1

Palmer, R. D., Bodine, D., Kumjian, M., Cheong, B., Zhang, G., Cao, Q., et al. (2011). Observations of the 10 May 2010 tornado outbreak using OU-PRIME: Potential for new science with high-resolution polarimetric radar. *Bulletin of the American Meteorological Society, 92,* 871–891. https://doi.org/10.1175/2011BAMS3125.1

Romine, G. S., Burgess, D. W., & Wilhemson, R. B. (2008). A dual-polarization-radar-based assessment of the 8 May 2003 Oklahoma City area tornadic supercell. *Monthly Weather Review*, *136*, 2849–2870. https://doi.org/10.1175/2008MWR2330.1

Rotunno, R., & Klemp, J. B. (1982). The influence of the shear-induced pressure gradient on thunderstorm motion. *Monthly Weather Review*, *110*, 136–151. https://doi.org/10.1175/1520-0493(1982)110<0136:TIOTSI>2.0.CO;2

Ryzhkov, A. V., Pinsky, M., Pokrovsky, A., & Khain, A. (2011). Polarimetric radar observation operator for a cloud model with spectral microphysics. *Journal of Applied Meteorology and Climatology*, *50*, 873–894.

Ryzhkov, A. V., Schuur, T. J., Burgess, D. W., & Zrnić, D. S. (2005). Polarimetric tornado detection. *Journal of Applied Meteorology*, *44*, 557–570.

Sachidananda, M., & Zrnić, D. (1986). Differential propagation phase shift and rainfall rate estimation. *Radio Science*, *21*, 235–247.

Seliga, T., & Bringi, V. (1976). Potential use of radar differential reflectivity measurements at orthogonal polarizations for measuring precipitation. *Journal of Applied Meteorology*, *15*, 69–76.

Seliga, T., & Bringi, V. (1978). Differential reflectivity and differential phase shift: Applications in radar meteorology. *Radio Science*, *13*, 271–275.

Thompson, R. L., Edwards, R., Hart, J. A., Elmore, K. L., & Markowski, P. (2003). Close proximity soundings within supercell environments obtained from the Rapid Update Cycle. *Weather and Forecasting*, *18*, 1243–1261. https://doi.org/10.1175/1520-0434(2003)018<1243:CPSWSE>2.0.CO;2

Thurai, M., & Bringi, V. (2005). Drop axis ratios from a 2D video disdrometer. *Journal of Atmospheric and Oceanic Technology*, *22*, 966–978.

Weisman, M., & Klemp, J. B. (1984). The structure and classification of numerically simulated convective storms in directionally varying wind shears. *Monthly Weather Review*, *112*, 2479–2498. https://doi.org/10.1175/1520-0493(1984)112<2479:TSACON>2.0.CO;2

Zittel, W. D., Cunningham, J. G., Lee, R. R., Richardson, L. M., Ice, R. L., & Melnikov, V. (2014). *Use of hydrometeors, Bragg scatter, and sun spikes to determine system ZDR biases in the WSR-88D fleet*. Paper presented at the 8th European Conference on Radar in Meteorology and Hydrology. Garmisch-Partenkirchen, Germany.